JMM

Improving Canny edge detection algorithm using fractional-order derivatives

Mina Mortazavi[†], Morteza Gachpazan[†∗], Mahmood Amintoosi[§]

[†]*Department of Applied Mathematics, Faculty of Mathematical Sciences, Ferdowsi University of Mashhad, Mashhad, Iran*
[§]*Faculty of Mathematics and Computer Science, Hakim Sabzevari University, Sabzevar, Iran*
Email(s): minamortazavi5@gmail.com, gachpazan@um.ac.ir, m.amintoosi@hsu.ac.ir

Abstract. One of the purposes of edge detection is to use methods that be able to process visual information according to human needs. Therefore, an edge detector is reliable when evaluated by measurement criteria before use in computer vision tools. These criteria compute the difference between the ground truth edge map (reference image) and the original image. In this study, we propose an improved Canny edge detection method based on the fractional-order operators to extract the ideal edge map. Then, by changing the hysteresis thresholds, the thin edges are obtained by filtering gradient calculations based on fractional-order masks. In addition, we employ common fractional-order derivative operators to extract the edge strength and enhance image edge contrast. The plotted curves of the edge detection criteria show that the obtained edge map of the proposed edge detection operator, which is considered to be the minimal rating of measurement, is visually and quantitatively closer to ground truth.

Keywords: Edge detection, hysteresis thresholds, fractional derivatives, Canny method, edge map.
AMS Subject Classification 2010: 68U10, 26A33.

1 Introduction

Edge detection is an important technique utilized in many applications in the field of image processing such as pattern recognition, medical image analysis, computer vision, and robotics. It is one of the most popular methods applied for feature extraction and object tracking, which considerably diminishes the processed data amount and maintains the structure of the image. The purpose of edge detecting is to find meaningful transfer information in an image and to identify discontinuities in the image where the color intensity of the image changes drastically [14]. Many effective methods have been suggested for edge detection in studies. Most of these methods are made based on integer-order derivatives, the

---

namely first-order derivative of the gradient operator, such as the Sobel [28], Prewitt [24], Canny [4], and Roberts [10], and second-order derivative of Laplacian operator [17], such as Laplacian of Gaussian. Usually, first-order derivative methods lead to thicker edges, which results in a lake of image details and second-order derivative methods could produce better edges but are very noise sensitive [2].

Utilizing fractional-order filters for edge detection has strongly solved these disadvantages [30]. This operator can maintain low-frequency components in smooth regions, preserve high-frequency edgy characteristics and also enhance medium-frequency texture details. In comparison with the property of the classical derivative, which leads to staircase artifact in the smooth areas, the fractional differential model is able to eliminate the block effect and maintain textures [32].

In the past three hundred years, fractional calculus has been an important branch of mathematics that is the generalization of integer derivatives and integration to non-integer arbitrary order. Leibniz had already discussed it in the eighteenth century, and other famous names of the past have studied and contributed to the development of fractional calculus in the field of pure mathematics [13]. The most popular used definitions of fractional differentiation are Riemann-Liouville, Grünwald- Letnikov, and Caputo [8]. Fractional calculus has played a fundamental role in several fields including automatic control, physics, signal, and image processing (see, e.g., [21–23, 31]). The fractional-order differential can enhance the edges and produce a texture more clear while maintaining the details information in smooth regions of the image [25].

Ref. [19] suggested a method of edge detection based on a fractional-order operator named CRONE, which can be remarkably improved the edge details and efficiency of noisy images. According to the numerical results, it can be seen that the proposed method generated fewer false negatives in the areas and also extracted edges with more precise details. In [1], authors proposed an approach for creating a fractional convolution mask based upon Riemann-Liouville fractional derivative. In [26], authors demonstrated that introduced method using fractional differential can be retained the low-frequency contour feature in smooth regions of the image, and can be preserved high-frequency marginal features in regions with a very diverse gray-level nonlinearly, it was indicated that by obtaining stronger edges and maintained the image texture it had better performance than the integer order derivatives. In the branches of image processing, fractional-based operators have been utilized for image resolution enhancement [33], image texture enhancement [26], image denoising [11], image segmentation [**?**], and so on.

In our paper, we accomplish two things. First, we propose a new way for edge detection so that the fractional-order derivative operator is combined in the Canny algorithm. Indeed, the derivative step in Canny operator is modified on the fractional-order gradient. The calculation of this gradient is obtained using common fractional-order derivative operators, including Grünwald-Letnikov (GL), Riemann-Liouville (RL), Caputo (C), Caputo-Fabrizio (CF), and Atangana and Baleanu in the Caputo sense (ABC) fractional-order integrals. Next, we utilize non-maximum suppression (NMS) and hysteresis thresholding to obtain the ideal edge map and to remove false edges respectively. In fact, this mathematical technique has been suggested to lay a base of our method for image enhancement such as preserving high-frequency edge and low-frequency contour features in a smooth region of the image. Second, we employ popular fractional-order derivative operators to be utilized for image edge detection and image edge contrast enhancement. Components of the gradient vector are calculated by applying fractional-based convolution mask. Then, we extract the edge strength by using the fractional gradient magnitude. In fact, we compare all the edge detection methods based on fractional-order derivatives and integer-order derivatives that researchers have presented in prior studies, both quantitatively and quali-

tatively, and determine the best method for achieving the most ideal edge strength. It should be noted that most researchers in their published works have evaluated the performance of their proposed method only with traditional methods based on integer derivatives. But here the performance of all non-integer derivative operators is evaluated with the performance of integer derivative operators. In addition, literature works published in recent years have used a determined α value to detect the edge using all comparative methods for all images. But here we get the optimal α value for each image block in accordance with the image structure in that block in different algorithms. We employ different measurement criteria such as PSNR, MSE, SSIM, and PR to evaluate the results of the experiments. Also, we utilize three types of datasets, including natural images, Chest X-Rays (CXR) images, and medical images to test the proposed method. The experimental results indicate that our proposed algorithm by using ABC fractional integral formulations with a non-local and non-singular kernel has a remarkable performance in improving the edge information, and gained an edge map closer to the ground truth image compared with other traditional integer-order methods and fractional-order derivatives methods.

The rest of this paper is arranged as follows: Section 2 presents a brief review of integer-order derivative edge detectors and popular fractional-order derivatives definitions. Section 3 first presents edge detection using the fractional derivative, then proposes a fractional Canny edge detector. The experimental results and the proposed methods' performance evaluation are discussed in Section 4. Finally, this study's conclusion presents in Section 5.

2 Background

In this section, we briefly review the methods of edge detection based on the integer-order derivative and basic definitions and theory of fractional calculus.

2.1 Review of edge detection operators

The edge goal is to recognize points of discontinuities in an image where image color intensity changes sharply, and these changes are detected by computing the integer first-order derivative or the gradient of the image intensity. The most common first-order derivative algorithms include Sobel, Prewitt, Laplacian, and Robert operators, demonstrated in Figure 1. The Roberts edge detector utilizes the distance between two diagonally neighbor pixels. The Roberts kernels are in action too small and cannot significantly recognize edges in the presence of noise. The Prewitt edge detector is obtained by approximating the first-order derivative based on the central difference algorithm. Another important edge detector is called the Sobel operator, which is obtained based on the finite-difference of the central. Unlike the Prewitt algorithm, this detector does give significance to pixels closer to the mask's center. The Sobel edge detector can give more detailed edge direction information, but this operator could generate many false edges with a thick edge width. The Sobel algorithm is more sensitive to the diagonal edges than to the horizontal and vertical ones, while the Prewitt edge detector is more sensitive to horizontal and vertical edges and to noise.

2.2 Basic definitions of the fractional calculus

The fundamental theory of fractional calculus is generalized from the theory of integer-order derivative, which extended from integer-order to any complex order or real.

-1	0	1
-2	0	2
-1	0	1

(a) $\mathscr{G}_{sx}$

1	2	1
0	0	0
-1	-2	-1

(b) $\mathscr{G}_{sy}$

-1	0	1
-1	0	1
-1	0	1

(c) $\mathscr{G}_{px}$

1	1	1
0	0	0
-1	-1	-1

(d) $\mathscr{G}_{py}$

0	-1	0
-1	4	-1
0	-1	0

(e) $\mathscr{G}_{LP}$

-1	-1	-1
-1	8	-1
-1	-1	-1

(f) $\mathscr{G}_{LP}$

1	0
0	-1

(g) $\mathscr{G}_{rx}$

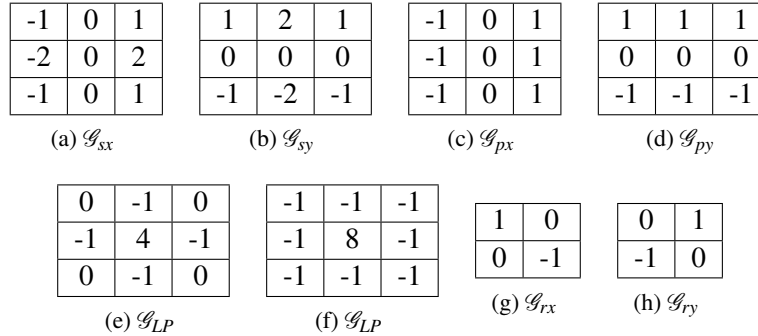| 0	1
-1	0

(h) $\mathscr{G}_{ry}$

Figure 1: The integer-order edge detection masks. (a,b) Sobel, (c,d) Prewitt, (e,f) Laplacian (g,h) Robert.

As we know, the image smooth region corresponds to the low-frequency component, in which adjacent pixels values are approximately the same. The region of the texture, which is the values of the neighboring pixels, has small variations corresponding to the medium frequency component. Edges and noise are in the form of high-frequency components, the adjacent image pixel values of which change sharply. Therefore, using the integer-order derivative approach to deal with the image smooth area, the texture details of the smooth area significantly lead to linear damping and the result is becoming close to zero. As a result, edge detectors based on traditional methods can not detect the details of the texture in the smooth area. In contrast, the low frequency of the signals is maintained by the fractional-order derivative [25]. The fractional-order α can constantly change, we can get the best edge information by choosing the best order α. We present primary definitions of Grünwald-Letnikov (GL), Riemann-Liouville (RL), Caputo (C), Caputo-Fabrizio (CF), and Atangana and Baleanu in the Caputo sense (ABC) fractional-order derivatives.

Definition 1. *[6] Assume for all $\alpha \in \mathscr{R}$, the signal $\Psi(\tau) \in [a,\tau]$ for $a < \tau$ and $a, \tau \in \mathscr{R}$ has the $\lceil \alpha \rceil$ order continuous differential. The GL fractional order derivative with $\alpha > 0$ can be defined as follows :*

$$_{a}^{GL}\mathfrak{D}_{\tau}^{\alpha}\Psi(\tau) = \lim_{h \to 0} \Psi_{h}^{(\alpha)}(\tau) = \lim_{h \to 0} h^{-\alpha} \sum_{r=0}^{\left[\frac{\tau-a}{h}\right]} (-1)^r \frac{\Gamma(\alpha+1)}{r!\Gamma(\alpha-r+1)} \Psi(\tau-rh). \tag{1}$$

Definition 2. *[1] Let for all $\alpha \in \mathscr{R}$, $a < \tau$ and $a, \tau \in \mathscr{R}$ has the $\lceil \alpha \rceil$ order continuous differential. The RL fractional order derivative of ψ of order α is described at a point $\tau(a,b)$ can be defined as follows:*

$$_{0}^{RL}\mathfrak{D}_{\tau}^{\alpha}\psi(\tau) = \frac{1}{\Gamma(\alpha)} \frac{d}{d\tau} \int_{a}^{\tau} \frac{\psi(\zeta)}{(\tau-\zeta)^{\alpha}} d\zeta, \ n-1 < \alpha \leq n. \tag{2}$$

Definition 3. *[27] Let $\Psi \in \mathscr{H}^1(a,b)$, $a < b$, $\alpha \in [0,1]$, $\mathscr{H}^1$ is the Sobolev space, the Liouville-Caputo fractional derivative of Ψ of order α is described at a point $\tau(a,b)$ as:*

$$_{0}^{C}\mathfrak{D}_{\tau}^{\alpha}\Psi(\tau) = \frac{1}{\Gamma(\alpha)} \int_{a}^{\tau} (\tau-\zeta)^{\alpha-1}\dot{\Psi}(\zeta) d\zeta, \ n-1 < \alpha \leq n. \tag{3}$$

Definition 4. *[3] Let $\Psi \in \mathscr{H}^1(a,b)$, $a < b$, $\alpha \in [0,1]$. The Caputo-Fabrizio derivative in Liouville-Caputo sense (CFC) of Ψ of order α is expressed at a point $\tau(a,b)$ as:*

$$_{0}^{CFC}\mathfrak{D}_{\tau}^{\alpha}\Psi(\tau) = \frac{(2-\alpha)\Omega(\alpha)}{2(1-\alpha)} \int_{0}^{\tau} exp\left[-\alpha\frac{(\tau-\zeta)}{1-\alpha}\right]\dot{\Psi}(\zeta) d\zeta, \ n-1 < \alpha < n. \tag{4}$$

Definition 5. *[9, 15] Let* $\Psi \in \mathcal{H}^1(a,b)$, $a < b$, $\alpha \in [0,1]$. *The Atangana-Baleanu fractional derivative with order α in Liouville-Caputo sense (ABC) is described as follows:*

$$_0^{ABC}\mathfrak{D}_\tau^\alpha \Psi(\tau) = \frac{\Omega(\alpha)}{(1-\alpha)} \int_0^\tau \mathfrak{E}_\alpha \left[-\alpha \frac{(\tau-\zeta)^\alpha}{1-\alpha} \right] \dot{\Psi}(\zeta)\,d\zeta, \ \ n-1 < \alpha \leq n. \tag{5}$$

In addition, the fractional integral of Atangana-Baleanu for a given function $\Psi(\tau)$ is represented as follows:

$$_0^{AB}\mathcal{I}_\tau^\alpha \Psi(\tau) = \frac{1-\alpha}{\Omega(\alpha)} \Psi(\tau) + \frac{\alpha}{\Gamma(\alpha)\Omega(\alpha)} \int_0^\tau \Psi(\zeta)(\tau-\zeta)^{\alpha-1}\,d\zeta, \ \ n-1 < \alpha \leq n, \tag{6}$$

where $\Omega(\cdot)$ function used in definitions mentioned is utilized as a normalized function, is given by follows:

$$\Omega(\alpha) = 1 - \alpha + \frac{\alpha}{\Gamma(\alpha)}, \ \ \Omega(0) = \Omega(1) = 1. \tag{7}$$

The use of the Mittag-Leffler function with order α is a keynote feature of the definition of ABC fractional derivative, expressed as:

$$\mathfrak{E}_\alpha(\tau) = \sum_{i=1}^\infty \frac{\tau^i}{\Gamma(\alpha i + 1)}, \ \ \ \alpha > 0. \tag{8}$$

3 The proposed edge detector

In the first section, we employ popular fractional-order derivative operators for image edge detection and image edge contrast enhancement. We obtain gradient operators by applying the convolution fractional-order masks. Then edge strength is extracted by the fractional gradient magnitude. The second section proposed the improved Canny algorithm in which the derivative step is modified on the fractional-order gradient so that it can produce an ideal edge map. The computation of this gradient leans on common fractional-order derivative operators, including GL, RL, C, CF, and ABC fractional-order integral formulations with non-singular and singular kernels.

3.1 Edge detection using fractional derivative

The fractional-order derivative operators can enhance the contrast edges and produce a texture more clear. The fractional-order differential can nonlinearly preserve the low-frequency contour information in smooth regions and also nonlinearly improve the high-frequency components like the edge.

To design masks, we utilize fractional discrete integrals and derivatives operators, the expansion of the image function is expressed as follows:

$$\mathcal{K}^\alpha \Psi(\tau) \approx \rho_0 \Psi(\tau) + \rho_1 \Psi(\tau-1) + \rho_2 \Psi(\tau-2) + \cdots, \tag{9}$$

where ρ_0, ρ_1, and ρ_2 are the value of the nonzero coefficients of expansion of the fractional differential definition of $\mathcal{K}^\alpha$.

Let $\Psi(x,y)$ is an image function in the Hilbert space, for the 2-D signal (x,y), the numerical algorithm of the fractional differentiation in the x-and y-directions respectively, can be approximated as:

$$^x\mathcal{K}_{GL}^\alpha \Psi(x,y) \approx \rho_0 \Psi(x,y) + \rho_1 \Psi(x-1,y) + \rho_2 \Psi(x-2,y) + \cdots, \tag{10}$$

$$^y\mathcal{K}_{GL}^\alpha \Psi(x,y) \approx \rho_0 \Psi(x,y) + \rho_1 \Psi(x,y-1) + \rho_2 \Psi(x,y-2) + \cdots.$$

We consider the mask structure introduced in [12], the coefficients of which are derived from fractional derivative operators. As a consequence of a 3×3 kernel constructed as follows:

$$\mathscr{M}_x^\alpha = \begin{bmatrix} -\rho_0 & 0 & \rho_0 \\ -\rho_1 & 0 & \rho_1 \\ -\rho_2 & 0 & \rho_2 \end{bmatrix}, \qquad \mathscr{M}_y^\alpha = \begin{bmatrix} -\rho_0 & -\rho_1 & -\rho_2 \\ 0 & 0 & 0 \\ \rho_0 & \rho_1 & \rho_2 \end{bmatrix}. \tag{11}$$

To enhance the accuracy of edge positioning, kernels (11) is rotating through $180°$ with the desired stage and can be expanded to eight directions. Therefore, edges are acquired using the input image convolution and rotated kernels. Rotating the kernel with step $45°$, eight various masks of the fractional derivatives to detect edges are considered, which these masks are implemented on input image with angles $0°$, $45°$, $90°$, $135°$, $180°$, $225°$, $270°$ and $315°$ (as shown in Figure 2). These kernels play an important role in extracting image details and features that can maintain texture and edge details.

These kernels are used to calculate the gradient operators $\mathscr{G}_x$ and $\mathscr{G}_y$. Then, the edge strength is extracted by using the gradient magnitude. Finally, we infer the gradient magnitude and orientation of the fractional gradient of an image $\Psi(x, y)$ as follows:

$$\mathscr{G}_x^\alpha(x, y) = \mathscr{M}_x^\alpha * \Psi(x, y), \ \ \mathscr{G}_y^\alpha(x, y) = \mathscr{M}_y^\alpha * \Psi(x, y),$$

$$FractionalEdge = \sqrt{(\mathscr{G}_x^\alpha(x, y))^2 + (\mathscr{G}_x^\alpha(x, y))^2},$$

$$\theta = \arctan\left(\frac{\mathscr{G}_y^\alpha}{\mathscr{G}_x^\alpha}\right).$$

In order to process a digital image, the nonlinear filter template is to move the mask along the image's pixels. The fractional filter on pixel (x, y) can be computed as follows:

$$\mathfrak{g}(x, y) = \sum_{i=-a}^{a} \sum_{j=-b}^{b} \mathscr{M}_x^\alpha(i, j) \Psi(x+i, y+j), \tag{12}$$

where $\Psi(x, y)$ and $\mathscr{M}_x^\alpha(i, j)$ are, respectively the value of a pixel and the value of the mask. The mask $\mathscr{M}$ is given into the $\mathfrak{m} \times \mathfrak{n}$ size, which $\mathfrak{m}$ and $\mathfrak{n}$ are taken odd. Then, $a = \frac{\mathfrak{m}-1}{2}$ and $b = \frac{\mathfrak{n}-1}{2}$.

$-\rho_0$	$-\rho_1$	$-\rho_2$
0	0	0
ρ_0	ρ_1	ρ_2

(a) $\mathscr{M}_{0°}^\alpha$

$-\rho_1$	$-\rho_2$	0
$-\rho_0$	0	ρ_2
0	ρ_0	ρ_1

(b) $\mathscr{M}_{45°}^\alpha$

$-\rho_0$	0	ρ_0
$-\rho_1$	0	ρ_1
$-\rho_2$	0	ρ_2

(c) $\mathscr{M}_{90°}^\alpha$

0	ρ_0	ρ_1
$-\rho_0$	0	ρ_2
$-\rho_1$	$-\rho_2$	0

(d) $\mathscr{M}_{135°}^\alpha$

ρ_0	ρ_1	ρ_2
0	0	0
$-\rho_0$	$-\rho_1$	$-\rho_2$

(e) $\mathscr{M}_{180°}^\alpha$

ρ_1	ρ_2	0
ρ_0	0	$-\rho_2$
0	$-\rho_0$	$-\rho_1$

(f) $\mathscr{M}_{225°}^\alpha$

ρ_0	0	$-\rho_0$
ρ_1	0	$-\rho_1$
ρ_2	0	$-\rho_2$

(g) $\mathscr{M}_{270°}^\alpha$

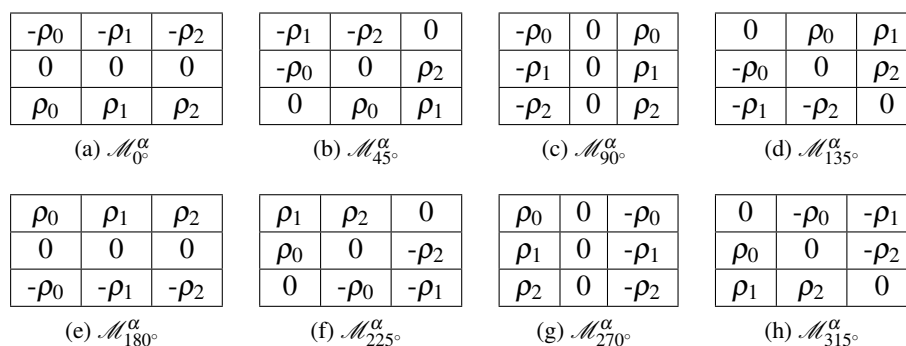| 0	$-\rho_0$	$-\rho_1$
ρ_0	0	$-\rho_2$
ρ_1	ρ_2	0

(h) $\mathscr{M}_{315°}^\alpha$

Figure 2: Fractional differential 3×3 mask on eight directions.

3.2 Fractional Canny edge detection

We propose a modified Canny edge detection algorithm in this section. In fact, the proposed method is a combination of the common fractional-order derivative operators such as GL, RL, C, CF, and ABC fractional-order integrals and Canny edge detector, in which we use the fractional order filter instead of an integer order filter for the gradient computation. The main purpose of this project is to modify the Canny algorithm and optimize the fractional filter. Flowchart 3 showed the overall framework of the proposed method. The implementation of the modified Canny edge detection algorithm followed four steps [4]:

Step1: Smoothing image: 2D Gaussian convolution is applied to the filter to smooth input image in order to remove the noise and details. The convolution filter size is usually much smaller than the real image. Fundamentally, the larger the size of the Gaussian filter, the more visible the smoothing blur, and localization error in the detected edges is increased, which can be written as:

$$G_{\sigma}(x,y) = \frac{1}{2\pi\sigma^2} exp(\frac{x^2+y^2}{2\sigma^2}), \quad \Psi_c(x,y) = \Psi(x,y) * G_{\sigma}(x,y). \tag{13}$$

Step2: Finding the intensity gradient: The edge strength is acquired by calculating the image intensity gradient. The edge magnitude can be got by calculating two fractional-order partial derivatives $\nabla_x^{\alpha}\Psi$ and $\nabla_y^{\alpha}\Psi$ and by convolving kernels $\mathcal{M}_x^{\alpha}$ and $\mathcal{M}_y^{\alpha}$ are given in (11), as follows:

$$\nabla_x^{\alpha}\Psi(x,y) = \mathcal{M}_x^{\alpha} * \Psi_c(x,y), \quad \nabla_y^{\alpha}\Psi(x,y) = \mathcal{M}_y^{\alpha} * \Psi_c(x,y), \tag{14}$$

$$mag(\Delta^{\alpha}\Psi) = \|\nabla^{\alpha}\Psi(x,y)\| = \sqrt{(\nabla_x^{\alpha}\Psi(x,y))^2 + (\nabla_y^{\alpha}\Psi(x,y))^2},$$

$$\theta = \arctan\left(\frac{\nabla_y^{\alpha}\Psi}{\nabla_x^{\alpha}\Psi}\right).$$

Step3: Non-maximum Suppression: The goal of the third step is to perform non-maximum suppression (NMS) to gain thin edges after specifying the edge directions. This is done to remove pixels that may not be part of an edge point. As a result, the output function (edge map) value at that point is set to be zero value. This operation will give into a binary image with "thin edges".

Step4: Thresholding with hysteresis: This step determined two high threshold (τ_H) and the low threshold (τ_L) values to keep the strong edges and remove the fake edges. These two threshold values identify all pixels in three classes such as strong, weak, and fake pixels. All pixels with an intensity gradient value greater than the high threshold are marked as "strong pixels", and thus will be preserved. But, if any pixels gradient value is smaller than the low threshold, the pixel is marked as "fake pixel", thus will be removed. However, weak pixels' gradient values between the low threshold and high threshold are considered. Finally, a series of lines remain between the two threshold values, which are divided into two categories, including the real pixels and fake pixels. If they are included in "strong pixels", they are considered part of the edge otherwise they must be suppressed.
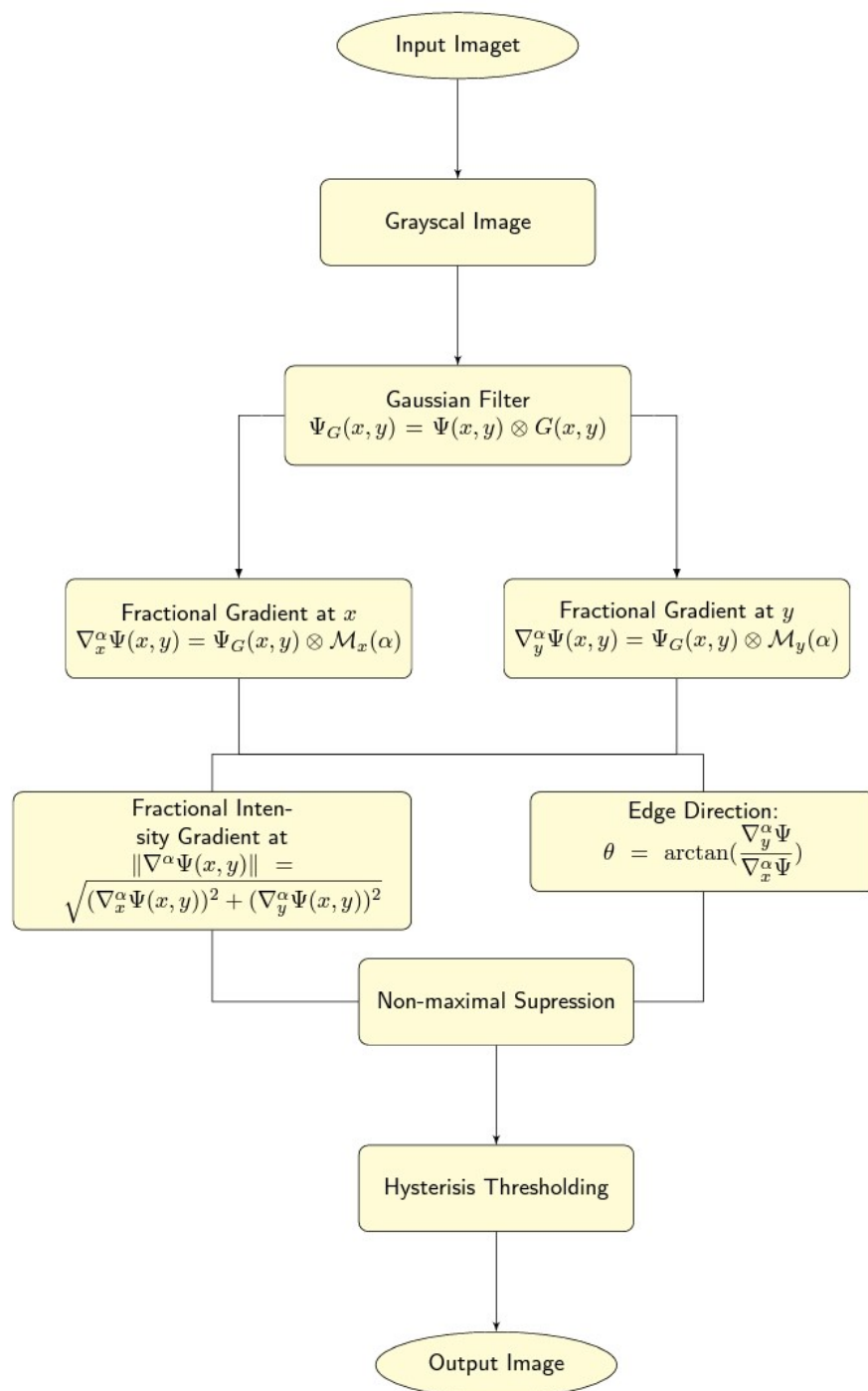
Figure 3: Flowchart of the fractional-order Canny edge detection algorithm.

4 Experimental results and discussions

In this section, we test the performance of the proposed method in view of visual quality and numerical quantities on a few datasets from various sources. In this research, the aim of the experiments given here is to acquire the best edge map by using the proposed algorithm with different fractional order masks such as Grünwald-Letnikov fractional derivative mask (GL) [6], Riemann-Liouville fractional derivative mask (RL) [1], Caputo fractional derivative mask (C) [20], Caputo-Fabrizio fractional derivative mask (CF) [16], masks based on ABC- fractional integral methods such as Grünwald-Letnikov fractional integral mask (GL-ABC) [12], Toufik-Atangana fractional mask (TA-ABC) [12], and Euler fractional mask (Eu-ABC) [12]. In order to analyze the performance of the proposed edge detection operator evaluation measures, each measure is compared by changing the hysteresis threshold of the thin edges computed with various fractional-order masks and integer-order masks such as Sobel.

Finally, compared to a ground truth image, the ideal edge map for measures corresponds to the wanted contour, in which the evaluation gains the minimal rating for the measures considered among the threshold thin gradient images. The size of the fractional differential mask is set to 3×3, and the value of the fractional power is considered $0.2 \leq \alpha < 1$. All experiments and implementation have been done utilizing Matlab 2018b on an Intel(R) Core i7-73687U personal computer of CPU @ 2.10 GHz, 4GB RAM, utilizing 32 bits Windows10.

4.1 Dataset

In our experiments, we utilize three types of datasets, including natural images, Chest X-Rays (CXR) images, and medical images. The natural image dataset is extracted from "The Berkeley Segmentation Dataset (BSDS300)" (https://www2.eecs.berkeley.edu/Research/Projects/CS/vision/grouping/segbench/). This dataset consists of 300 natural images with their manual segmentations divided into 200 training images and 100 testing images. It includes also human annotations that serve as ground truth for fairness of boundary detection [18]. The size of the BSDS300 images and its ground truth is 481×321 pixels. Figure 4 demonstrates samples of the selected images from BSDS300.

Chest X-Rays (CXR) images dataset is categorized into COVID-19, Viral Pneumonia, and Normal (healthy), Lung Opacity images, which are extracted from Tawsifurrahman's Kaggle dataset (https://www.kaggle.com/tawsifurrahman/COVID19-radiography-database/) and Tawsifurr's dataset [7, 29]. The size of the CXR images is 299×299. In total 21,165 images are collected in the X-Ray database, which includes 3616 COVID-19 positive cases, 10192 Normal images, 6012 Lung Opacity (Non-COVID lung infection), and 1345 Viral Pneumonia images. Here we select COVID-19 images from Radiopedia which belongs to a patient 80-year-old female (https://radiopaedia.org/cases/aspiration-pneumonia-5) and Cohens dataset [5]. The size of positive (COVID-19) images is resized to 512×512. Figure 5 demonstrates samples of the selected X-Rays images. Medical images contain Aneurysms images, X-ray hand images, and CT images are extracted from Radiopedia (https://radiopaedia.org/cases?lang=us&page=1), as shown in Figure 6.

4.2 Quantitative Measures of Analysis

To make the quantitative performance comparison of the edge detectors, we employ four different measurement criteria, such as Mean Square Error (MSE), Peak Signal-to-Noise Ratio (PSNR), Structural
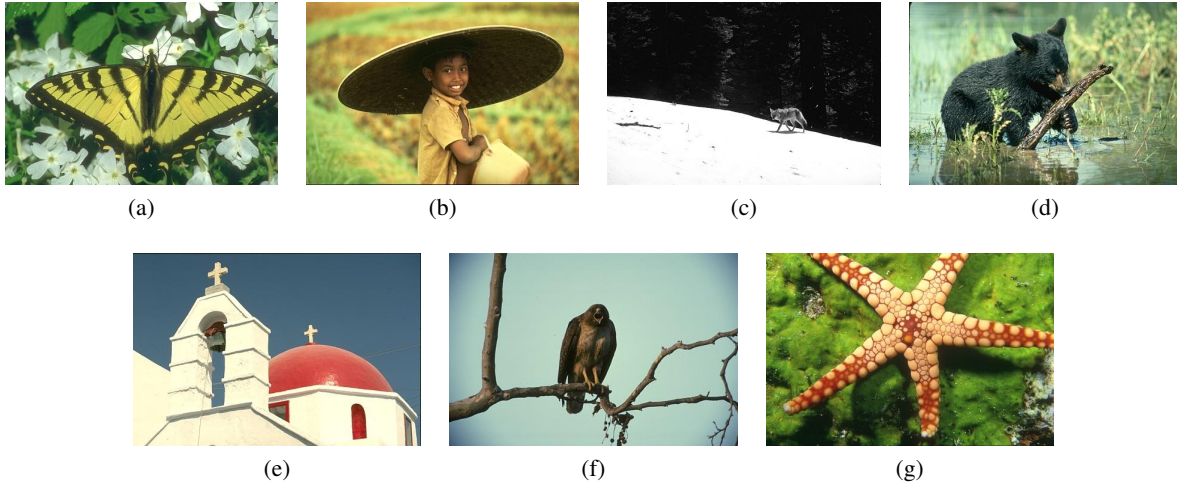
Figure 4: Sample images for testing comparison from BSDS300; (a) "35010" image , (b) "189011" image, (c) "167062" image, (d) "159091" image, (e) "118035" image, (f) "42049" image, (g) "12003" image.
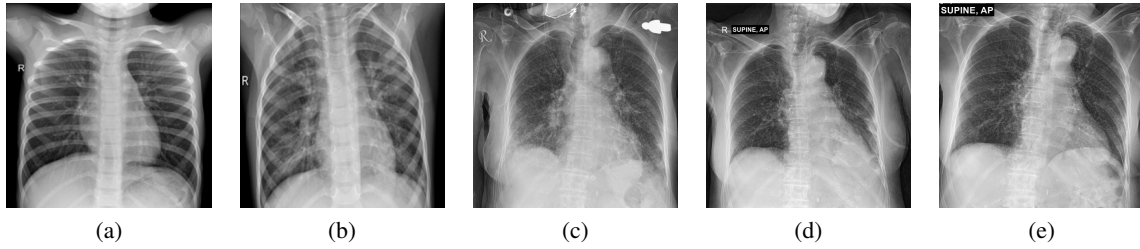

Figure 5: Sample images chest X-Ray images from a patient ($\sharp$5) for testing comparison. This 80-year-old female survived a COVID-19 infection [5, 7]; (a) Normal image, (b) Viral Pneumonia image, (c-e) COVID-19 images: (c) Day 1, (d) Day 10, (e) Day 24.

Similarity Index (SSIM), and Performance Ratio (PR). In each sample, the behavior of the computed values of four metrics is displayed for various orders α. Anyhow, computing these metrics requires ground truth as reference edge images that are annotated manually by humans. The MSE and PSNR are computed as follows:

$$MSE = \frac{1}{MN} \sum_{i=1}^{M} \sum_{j=1}^{N} \left(\Psi(i,j) - \mathscr{V}(i,j) \right)^2,$$

$$PSNR = 10 \log_{10} \left(\frac{255^2}{MSE} \right),$$

where Ψ is the original image, and $\mathscr{V}$ is the recovered image. The PSNR value depends wholly on the mask window size and the fractional-order α value. As you know the higher PSNR and a lower MSE illustrates, the better recovery performance of the proposed fractional-order masks obtains.

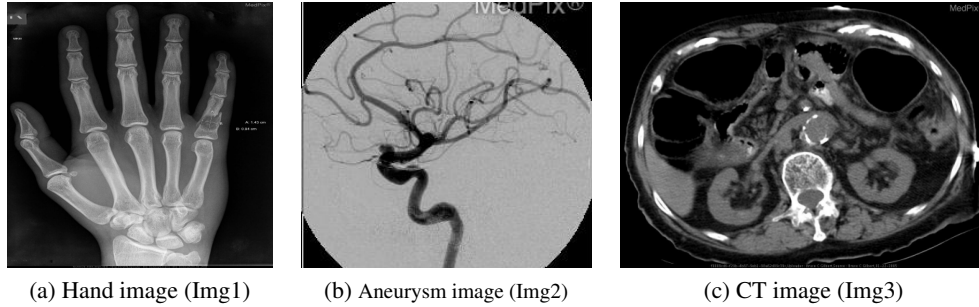(a) Hand image (Img1) (b) Aneurysm image (Img2) (c) CT image (Img3)

Figure 6: Sample medical images for testing comparison were extracted from Radiopedia.

SSIM index is utilized to measure the similarity between two images. SSIM is a full reference criterion to measure image quality employing an initial image with perfect quality as a reference. The SSIM values range expands between -1 and $+1$ and only in the case equals 1 if the two images are identical. The SSIM formulation is expressed as:

$$SSIM(\mathscr{A},\mathscr{B}) = \frac{(2\mu_{\mathscr{A}}\mu_{\mathscr{B}}+\mathscr{C}_1)(2\sigma_{\mathscr{A}\mathscr{B}}+\mathscr{C}_2)}{(\mu_{\mathscr{A}}^2+\mu_{\mathscr{B}}^2+\mathscr{C}_1)(\sigma_{\mathscr{A}}^2+\sigma_{\mathscr{B}}^2+\mathscr{C}_2)},$$

$$\sigma_{\mathscr{A}\mathscr{B}} = \left(\frac{1}{N-1}\sum_{i=1}^{N}(\mathscr{A}_i-\mu_{\mathscr{A}})(\mathscr{B}_i-\mu_{\mathscr{B}})\right),$$

where $\mu_{\mathscr{A}}$ and $\mu_{\mathscr{B}}$ are the mean intensity of $\mathscr{A}$ and $\mathscr{B}$, respectively, $\sigma_{\mathscr{A}}^2$ and $\sigma_{\mathscr{B}}^2$ are the variance of of $\mathscr{A}$ and $\mathscr{B}$, respectively, $\sigma_{\mathscr{A}\mathscr{B}}$ is the covariance, and $\mathscr{C}_1$ and $\mathscr{C}_2$ are two small constants.

PR (Performance Ratio of True to False Edges) is another criterion for evaluating edge detection. It is computed using a ground truth (G_t) map edge, where "True Edges" are edge pixels recognized as edges, while "False Edges" are the sum of non-edge pixels recognized as non-edge pixels. Its formula is defined as follows:

$$PR = \frac{TrueEdges}{FalseEdges} \times 100.$$

4.3 Qualitative Comparison

In this work, the experimental results are divided into two sections. In Section 4.3.1, we extract edge strength by using integer and fractional gradient magnitude. Then, the performance of the obtained results of all methods based on integer-order and fractional-order derivatives are compared and evaluated in terms of quantitative and qualitative analysis. In Section 4.3.2, we utilize the kernels based on fractional-order operators in Canny edge detection algorithm. Then, changing the hysteresis thresholding, the best edge map is acquired by using fractional gradient computations and compared to the ground truth. The performance of the results is evaluated in terms of quantitative and qualitative analysis on the Berkeley segmentation dataset and medical image dataset.
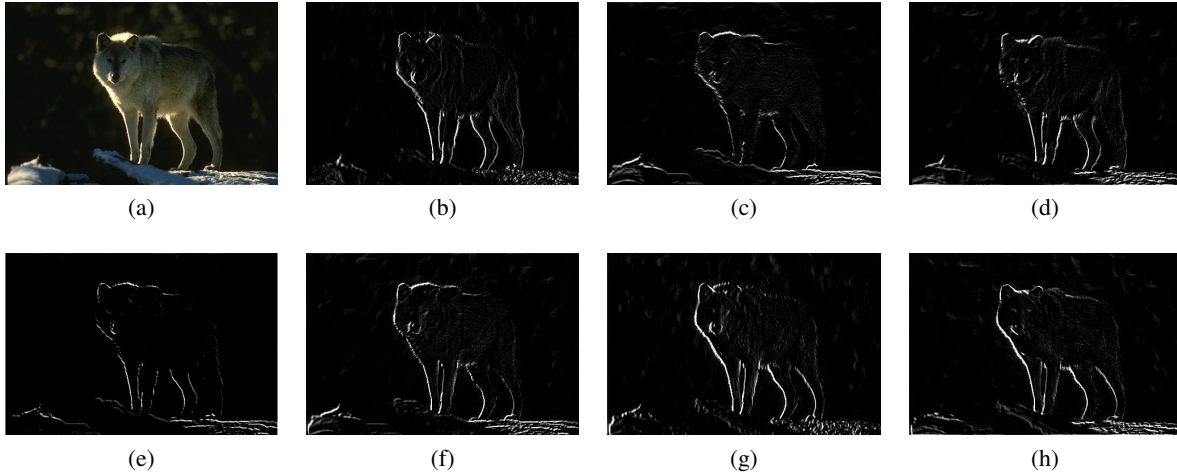
Figure 7: Qualitative comparison of the edge strength obtained using GL-ABC fractional order mask on eight directions on image "42078" with $\alpha = 0.9$; (a) Original image, (b) fractional $\mathcal{M}_x^{0.9}$ gradient in x direction, (c) fractional $\mathcal{M}_y^{0.9}$ gradient in y direction, (d) fractional $\mathcal{M}_\theta^{0.9}$ gradient in $\theta = 45°$ direction, (e) fractional $\mathcal{M}_\theta^{0.9}$ gradient in $\theta = 135°$ direction, (f) fractional $\mathcal{M}_\theta^{0.9}$ gradient in $\theta = 225°$ direction, (g) fractional $\mathcal{M}_\theta^{0.9}$ gradient in $\theta = 270°$ direction, (h) fractional $\mathcal{M}_\theta^{0.9}$ gradient in $\theta = 315°$ direction.

4.3.1 Experiment 1: Edge Strength Extracted by Integer and Non-integer Operators

In this section, we utilize non-integer edge detectors such as CF [16], RL [1], GL-ABC [12], TA-ABC [12], and Eu-ABC [12] and integers edge detectors such as Roberts [10], Prewitt [24], Sobel [28], Canny [4] to detect image edge strength and enhance image edge contrast. Here, first the gradient components by applying the convolution fractional order masks are calculated. Then, we extract the edge strength by using the fractional gradient magnitude. Therefore, we compare all the non-integer and integer edge detectors both quantitatively and qualitatively, and determine the best method for achieving the most ideal edge strength. Before describing more details about experiments on the aforementioned databases, we present an example in Figure 7 to demonstrate the results of the fractional mask in eight directions in Figure 2. In this test, we use the GL-ABC fractional operators with different values of α on the image "42078", the test image used in this experiment is selected from dataset BSDS300.

For the eyes qualitative analysis, Figure 8 indicates a comparison of the performance of all edge detectors. It should be noted that to avoid the crowded experiment result section and to avoid the paper being long, we provid the rest of the numeric results in the Supplementary Materials file. Please see Section 1 of the Supplementary Material file. Figure 8 demonstrates that integer and non-integer order edge detectors both can find the edge. But when dealing with some points, they can not differentiate between the image's main part and its background. Figure 8(c-f) demonstrates the results of integer order masks on "159091" image. It can be observed that Roberts operator is poorly detected low-frequency characteristic and is found discontinuity of the edge during the operation. The Canny operator is an ideal edge detection method, but for a better result, it needs a larger filter which may cause more image information to be lost. In addition, Figure 8(g-k) indicates the results of fractional order masks. As it can be seen in Figure 8(h) the RL operator maintained well low-frequency characteristics ineffective
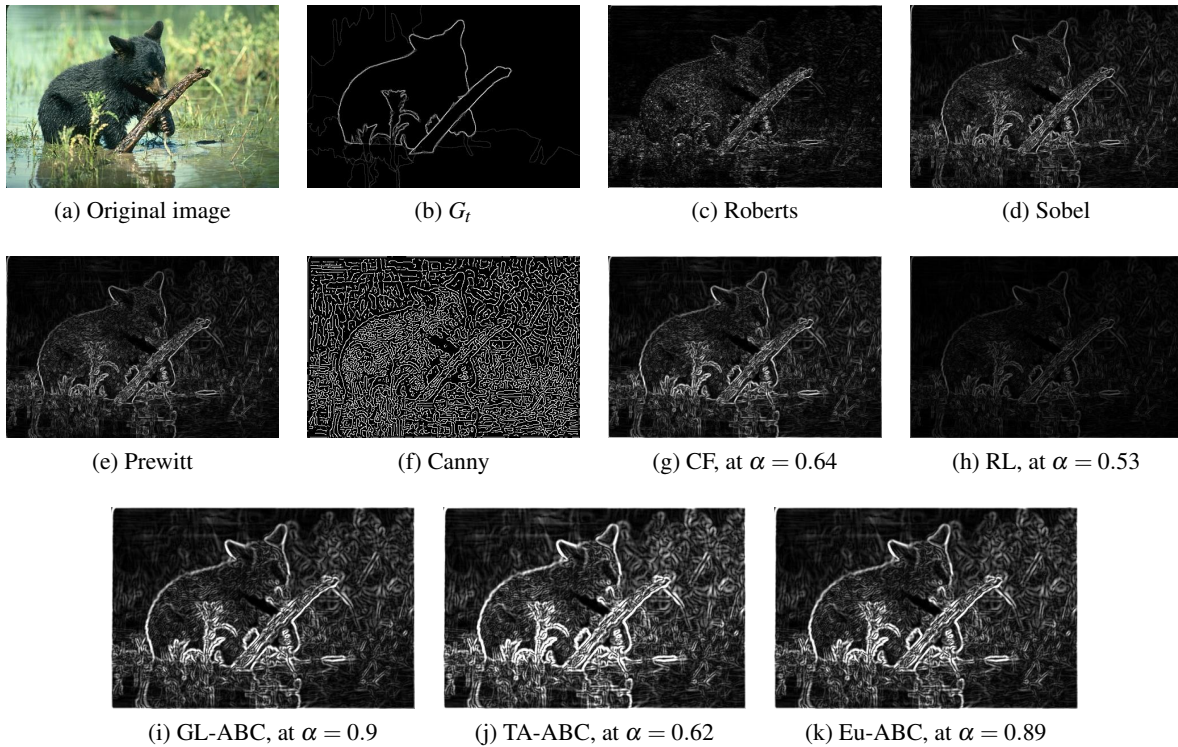
(a) Original image   (b) G_t (c) Roberts   (d) Sobel

(e) Prewitt   (f) Canny   (g) CF, at $\alpha = 0.64$ (h) RL, at $\alpha = 0.53$

(i) GL-ABC, at $\alpha = 0.9$ (j) TA-ABC, at $\alpha = 0.62$ (k) Eu-ABC, at $\alpha = 0.89$

Figure 8: Qualitative comparison of the edge strength obtained using various edge detectors on "159091" image.

regions and did not effectively consider the complexity of the local texture. Therefore, it only led to the outer edges. The same observations can be expressed for the rest of the figures in Section 1 of the Supplementary Material file. It seems that the TA-ABC fractional mask has obtained the best output compared to the other methods. The operators based on the ABC-fractional integral take into account high and low-frequency features compared to other integer and non-integer differential algorithms. As a result, the fractional-order filters based on the ABC-fractional differential operator can be detected the whole of the important image details. They generate sharper, more accurate, and thicker edges, and moreover can remove the false negatives in the textured areas, increasing the image edge contrast.

4.3.2 Experiment 2: Edge Map Extracted By Using Hysteresis Thresholding

The goal of the experiments presented in this study is to get the best edge map in the proposed way, and prove the performance of the proposed algorithm for accurate detection of edges in different databases. In order to explore the efficiency of edge detection evaluation measures, we compare each measure by changing the threshold of the thin edges with different edge detectors: Prewitt [24], Sobel [28], Canny [4], GL [6], C [20], CF [16], RL [1], GL-ABC [12], TA-ABC [12], and Eu-ABC [12] operators. Next, each image of the selected dataset is processed by the mentioned algorithms, then the acquired ideal edge map is compared with ground truth image to get the minimum score for measurement criteria. On
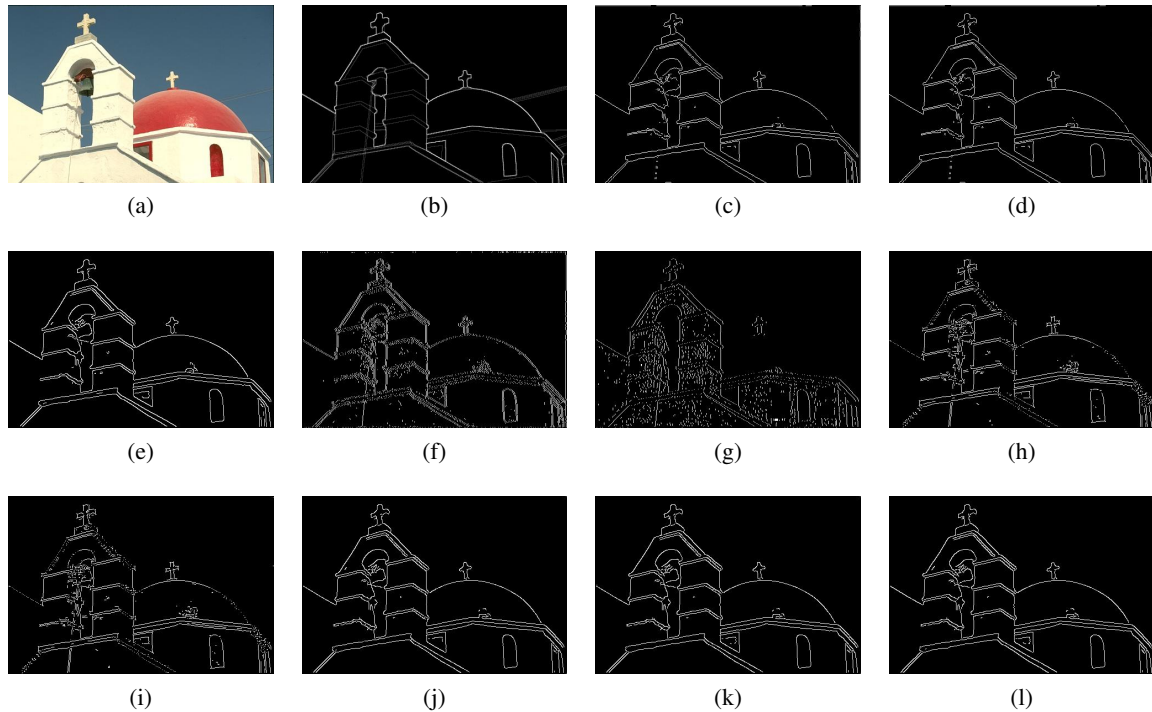
Figure 9: Qualitative comparison of edge map obtained by NMS into Canny operator using various edge detectors on "118035" image with Hysteresis thresholding values, $\tau_H = 0.15$ and $\tau_L = 0.08$, (a) Original image, (b) Ground Truth(G_t), (c) Prewitt, (d) Sobel, (e) Canny+sobel, (f-l) Result using our proposed method: (f) Canny+GL at ($\alpha = 0.98$), (g) Canny +C at ($\alpha = 0.2$), (h) Canny+CF at ($\alpha = 0.92$), (i) Canny+RL at ($\alpha = 0.2$), (j) Canny+GL-ABC at ($\alpha = 0.2$), (k) Canny+TA-ABC at ($\alpha = 0.2$), (l) Canny+Eu-ABC at ($\alpha = 0.2$).

the other hand, as we said, all the tested methods are based on the Canny algorithm process. Therefore, all the parameters used in this process must be fixed, and we also consider the lower and higher threshold values to be the same for all algorithms. In Figure 9, we can observe the performance of the kernels based on ABC- fractional integral and the rest of fractional and integer-order kernels into the Canny algorithm. The rest of the test results in Section 1 of the Supplementary Materials file are inserted. As you can see from the resulting tests, apparently all edge detectors detected more edges than the ground truth image. Human edge images (ground truth images) have been manually annotated with strong edges by multiple human observers, while Edge detectors extract all discontinuities, including weak edges, in an image.

In Figure 9, we can apperceive that the combination of Canny algorithm with fractional edge detectors especially GL and C operators produce external lines, lose texture details, the effect of edge gradient leads to artifacts in edge, generate thick edges, create false negative in the textured areas. Whereas GL-ABC, TA-ABC, and Eu-ABC edge detectors have a good performance on all images and improve image objective quality remarkably, obtain the thin edges by filtering gradient computations based on ABC-fractional integral kernels, extract better edge maps than other detectors by changing the hysteresis thresholding, reduce the effect of artifacts on the edges, suppress weak edges to a certain extent and
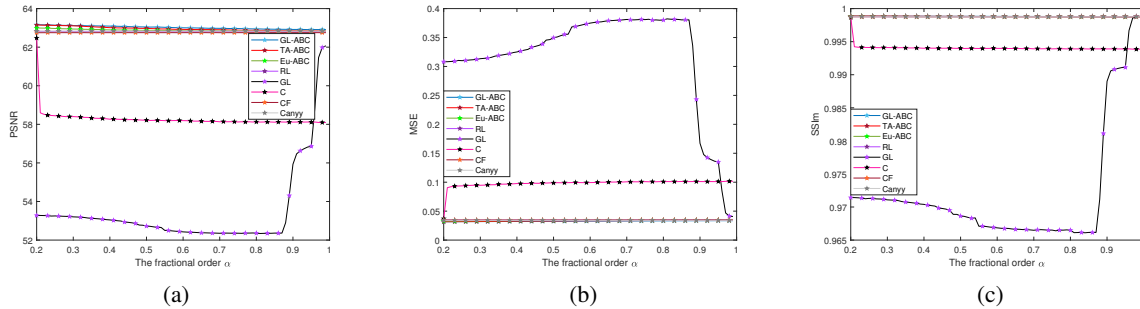
Figure 10: Image "118035": Comparison of edge detection evaluation with different α's for three measures: (a) PSNR, (b) MSE, (c) SSIM.

debilitate false negatives in the textured areas. By choosing the best α order, the false negatives in the textured areas are removed and the resulting edge map is closer to human edge images.

4.4 Quantitative Comparison

The plotted curve in Figure 10 exhibits the evolution of the numerical simulations of MSE, SSIM, and PSNR for the proposed edge detector with fractional masks in Section 4.3.2, in which various colors are utilized to distinguish different filters. Since the detailed results for all images make the paper very long, we insert the rest of the graphs in Section 2 of the Supplementary Materials file. The graph 10 illustrates that our proposed method based on ABC- fractional order masks have the highest performance for the small values of $\alpha = 0.2$ because of better localization of edges. As you can notice from all graphs, by increasing the fractional-order α from 0.2 to 1, the error indicated by the MSE metric increases, and the SSIM and PSNR decrease to reach the worst value of 1, which corresponds to the integer-order derivative. For all experiments, the PSNR, SSIM, PR, and MSE values for the GL-ABC fractional operator with Canny in Section 4.3.2 have superiority over other operators illustrating more likeness between ground truth and the edge map obtained from GL-ABC mask.

For the quantitative analysis, Tables 1 and 2 exhibit the comparison results of texture analysis for different masks in terms of different measure criteria for all considered datasets. Each cell demonstrate the value of the corresponding criteria for the mentioned image and method. The method which won first place is highlighted in bold, and the second place is highlighted in underlined. Table 1 gives the numerical simulations using the MSE, SSIM, PR, and PSNR metrics on each one of the natural images presented in Figure 4 and their ground truth. By the definition of MSE, we as know that the smaller the MSE is, the more similar the edge map obtained by non-maximum suppression and ground truth, and also compatible with the human visual system. In addition, the computed PR values illustrate that the GL-ABC, TA-ABC, and Eu-ABC masks detected more edges than the comparative masks.

Tabel 2 evaluates measure criteria results for CXR images and medical images presented in Figures 5 and 6, respectively. The numerical results confirm the ABC-fractional-order filters excellence with less MSE and higher PSNR than the integer and non-integer order derivative filters. It should be noted that the computational cost of the ABC- fractional order masks in this manuscript is equal to the corresponding costs in other fractional order masks. Based on the obtained results, we can conclude that the proposed

approach with ABC fractional integral masks with a non-local and non-singular kernel have achieved the best results in terms both visually and qualitatively than other approaches.

4.5 Advantages and Disadvantages of Edge Detector

There are disadvantages and advantages to using the integer-order differential methods with edge detection operators. There are disadvantages and advantages to using the integer-order differential methods with edge detection operators. The primary advantages of integer-order algorithms are simplicity .These algorithms could enhance the edge information effectively. The major disadvantages of these classical operators are sensitivity to the noise, in the detection of the edges and their orientations and the inaccuracy. Using the fractional calculus, one can overcome the existing problems in the well-known masks such as Canny, Prewitt, and Sobel. The primary advantages of fractional-order operators are flexibility in choosing the fractional derivative order. The fractional-order parameter gives an extra degree of freedom in designing different masks, and the order α can continuously change, we can obtain the best image edge information by adjusting the value of α in our experiments. The disadvantages of these fractional-order operators are that the numerical implementation of fractional order calculus is very complicated. The use of the fractional differential in the convolution mask can be devastating if not attentively constructed.

5 Conclusion

This manuscript is divided into two parts. In the first part, we extract the edge strength map by using the gradient magnitude. Indeed, the image gradient is calculated by the convolution masks of the fractional-order operators. In the second part, we introduce a modified Canny edge detection algorithm. In fact, the introduced method is a combination of the fractional-order operators and Canny edge detection algorithm. Here, after computing gradient magnitude (edge strength), we employ non-maximum suppression (NMS) to obtain the ideal edge map. Finally, hysteresis thresholding is utilized to eliminate false edges. In this work, we analyze the performance evaluation of the proposed method compared to other methods from the view of visual and quantitative quality on three types of datasets, including natural images, CXR images, and medical images. The measurement criteria used to evaluate the resulting tests are PSNR, MSE, SSIM, and PR. In the first experiment, we observe that the obtained masks based on ABC-fractional integral formulation enhance image contrast while preserving the smooth area of the image, and also generate sharp and highlighted edges compared to other edge detectors. In the second experiment, we observe that the proposed method with ABC-fractional order masks suppress the false edges, by choosing the best α order and hysteresis thresholding, it has produced strong edges and thin edges. The resulting edge map is visually closer to the ground truth image. Finally, we conclude that the efficiency of the GL-ABC, TA-ABC and Eu-ABC fractional-order operators is superior to other comparative operators.

References

[1] P. Amoako-Yirenkyi, J.K. Appati, I.K. Dontwi, *A new construction of a fractional derivative mask for image edge analysis based on riemann-liouville fractional derivative*, Adv. Differ. Equ. **2016** (2016) 1–23.

Table 1: Comparison of quantitative performance of different edge detectors on the nature image 4.

Method \ Image	Measures	"35010"	"42049"	"189011"	"167062"	"118035"	"12003"	"159091"
Prewitt	PSNR	60.6887	63.9337	64.4683	67.2504	62.7784	61.4480	63.2873
	MSE	0.0559	0.0265	0.0234	0.0123	0.0346	0.0470	0.0307
	SSIM	0.9981	0.9993	0.9992	0.9996	0.9990	0.9980	0.9989
	PR	12.0814	15.7919	5.9794	8.2221	11.6522	8.8784	8.0686
Sobel	PSNR	60.6245	63.8921	64.6750	68.6628	62.7620	61.2555	63.4567
	MSE	0.0568	0.0267	0.0223	0.0089	0.347	0.491	0.0296
	SSIM	0.9981	0.9993	0.9992	0.9997	0.9990	0.9979	0.9989
	PR	12.2539	15.8362	5.6932	7.7767	11.8948	9.2115	7.8456
Canny+Sobel	PSNR	59.8963	63.7807	65.0292	69.1537	62.8324	61.9412	64.3651
	MSE	0.0671	0.0274	0.0206	0.008	0.0341	0.0419	0.0240
	SSIM	0.9975	0.9992	0.9992	0.9997	0.9988	0.9982	0.9990
	PR	**14.9279**	17.211	5.6405	8.2771	14.4659	9.664	8.1931
Canny+GL	PSNR	60.5912	64.0733	65.5335	65.9153	61.9806	60.4332	63.4313
	MSE	0.0572	0.0257	0.0183	0.0168	0.0415	0.0593	0.0297
	SSIM	0.9981	0.9992	0.9993	0.9995	0.9988	0.9975	0.9988
	PR	11.0811	11.0946	4.2865	6.0546	14.6172	9.175	6.8642
Canny+C	PSNR	60.0244	64.5330	65.3821	66.8140	62.4776	60.9374	62.1386
	MSE	0.0652	0.0231	0.0190	0.0136	0.0370	0.0528	0.0401
	SSIM	0.9975	0.9992	0.9991	0.9997	0.9987	0.9980	0.9984
	PR	6.9951	8.2765	3.1399	2.5901	7.9008	7.2589	6.0796
Canny+CF	PSNR	60.6025	64.1504	65.3348	68.6360	62.7502	61.0526	64.1881
	MSE	0.0571	0.0252	0.0192	0.009	0.0348	0.0514	0.0250
	SSIM	**09981**	0.9993	0.9993	0.9997	0.9988	0.9979	0.9990
	PR	11.3147	14.0543	2.7365	7.5477	12.3465	9.6066	7.1893
Canny+RL	PSNR	60.7762	64.2294	65.4198	68.7926	62.8195	61.2986	64.3790
	MSE	0.0548	0.0247	0.0188	0.0087	0.0342	0.0486	0.0239
	SSIM	0.9981	0.9993	0.9993	0.9997	0.9988	0.9980	0.9990
	PR	10.8927	13.7856	4.5632	7.3941	12.1609	9.1121	6.8882
Canny+GL-ABC	PSNR	**60.8741**	**64.9374**	**65.8900**	<u>69.2291</u>	**63.1620**	**61.9594**	**64.4040**
	MSE	**0.0536**	**0.0210**	**0.0169**	<u>0.0078</u>	**0.0316**	**0.0417**	**0.0238**
	SSIM	0.9980	**0.9994**	**0.9993**	0.9997	**0.9989**	**0.9982**	**0.9992**
	PR	14.2191	17.4936	**6.2465**	**8.3412**	<u>14.6353</u>	9.748	**8.2793**
Canny+TA-ABC	PSNR	<u>60.8465</u>	<u>64.8403</u>	<u>65.7813</u>	**69.2646**	<u>63.1519</u>	<u>61.9118</u>	<u>64.3216</u>
	MSE	<u>0.0539</u>	<u>0.0215</u>	<u>0.0173</u>	**0.0077**	<u>0.0317</u>	<u>0.0422</u>	<u>0.0242</u>
	SSIM	<u>0.9980</u>	0.9994	<u>0.9993</u>	**0.9997**	0.9989	0.9982	<u>0.9991</u>
	PR	14.2576	<u>17.6734</u>	<u>6.2436</u>	8.2277	14.5819	<u>9.767</u>	<u>8.0868</u>
Canny+Eu-ABC	PSNR	60.5212	64.4976	65.6505	69.2404	62.9931	61.8902	64.3216
	MSE	0.0581	0.0233	0.0178	0.0078	0.0329	0.0424	0.0242
	SSIM	0.9978	<u>0.9993</u>	0.9993	0.9997	<u>0.9988</u>	<u>0.9981</u>	0.9991
	PR	<u>14.5601</u>	**17.7972**	6.2173	<u>8.3059</u>	**14.7418**	**9.9088**	8.037

[2] T. Bento, D. Valério, P. Teodoro, J. Martins, *Fractional order image processing of medical images*, J. Appl. Nonlinear Dyn. **6** (2017) 181–191.

[3] M. Caputo, M. Fabrizio, *A new definition of fractional derivative without singular kernel*, Prog. Fract. Differ. Appl. **1** (2015) 73-85.

[4] J.F. Canny, *A computational approach to edge detection*, IEEE Trans. Pattern Anal. Mach. Intell. **6** (1986) 679–698.

Table 2: Comparison of quantitative performance of different edge detectors on the images (5 and 6)

Method \ Image	Normal image		Vital Pneumonia image		COVID-19 image		Img1		Img2	
	PSNR	MSE	PSNR	MSE	PSNR	MSE	PSNR	MSE	PSNR	MSE
Prewitt	53.1148	0.2930	53.5703	0.9654	53.1044	0.3207	57.0477	0.1293	52.5600	0.3635
Sobel	53.4923	0.2933	53.5690	0.2881	53.1115	0.3201	57.0517	0.1292	52.5640	0.3631
Canny+Sobel	53.5117	0.2920	53.5473	0.2896	53.1065	0.3205	57.0025	0.1307	52.5833	0.3615
Canny+CF	53.4969	0.2930	53.5621	0.2888	53.1148	0.3199	57.0525	0.1292	52.5805	0.3618
Canny+RL	53.4976	0.2929	53.5668	0.2883	53.1194	0.3196	57.0519	0.1292	52.5804	0.3618
Canny +GL-ABC	**53.5137**	**0.2918**	**53.5729**	**0.2879**	**53.1226**	**0.3193**	57.0525	0.1292	52.5787	0.3619
Canny+TA-ABC	<u>53.5132</u>	<u>0.2919</u>	<u>53.5669</u>	<u>0.2883</u>	<u>53.1218</u>	<u>0.3194</u>	<u>57.0660</u>	<u>0.1288</u>	**52.5866**	**0.3613**
Canny+Eu-ABC	53.5075	0.2922	53.5589	0.2888	53.1191	0.3196	**57.0688**	**0.1287**	<u>52.5861</u>	<u>0.3614</u>

[5] J.P. Cohen, P. Morrison, L. Dao, K. Roth, T.Q. Duong, M. Ghassemi, *Covid-19 image data collection: Prospective predictions are the future*, https://arxiv.org/abs/2006.11988.

[6] X. Chen, X. Fei, *Improving edge-detection algorithm based on fractional differential approach*, International Conference on Image, Vision and Computing, Shanghai, China, August, **50** 2012 25–26.

[7] M.E. Chowdhury, T. Rahman, A. Khandakar, R. Mazhar, M.A. Kadir, Z.B. Mahbub, K.R. Islam, M.S. Khan, A. Iqbal, N. Al Emadi, M.B. Ibne Reaz, T.I. Islam *Can AI help in screening viral and COVID-19 pneumonia*, IEEE Access **8** (2020) 132665–132676.

[8] K. Diethelm, N.J. Ford, *Analysis of fractional differential equations*, J. Math. Anal. Appl. **265** (2002) 229–248.

[9] J. Djida, A. Atangana, I. Area, *Numerical computation of a fractional derivative with non-local and non-singular kernel*, Math. Model. Nat. Phenom. **12** (2017) 4–13.

[10] P. Elias, L.G. Roberts, *Machine perception of three-dimensional solids*, PhD thesis, Massachusetts Institute of Technology, 1963.

[11] B. Ghanbari, A. Atangana, *A new application of fractional atangana baleanu derivatives: designing abc-fractional masks in image processing*, Phys. A: Stat. Mech. Appl. **542** (2020) 123516.

[12] B. Ghanbari, A. Atangana, *Some new edge detecting techniques based on fractional derivatives with non-local and non-singular kernels*, Adv. Differ. Equ. **2020** (2020) 1.

[13] R. Gorenflo, F. Mainardi, *Fractional calculus: Integral and differential equations of fractional order: From, Fractals and fractional calculus*, Contin. Mech. **378** (2008) 223–276.

[14] M. Gudmundsson, E.A. El-Kwae, M.R. Kabuka, *Edge detection in medical images using a genetic algorithm*, IEEE Trans. Med. Imaging **17** (1998) 469–474.

[15] H.J. Haubold, A.M. Mathai, R.K. Saxena, *Mittag-leffler functions and their applications*, J. Appl. Math. **2011** (2011).

[16] J. Lavín-Delgado, J. Solís-Pérez, J.F. Gómez-Aguilar, R.F. Escobar-Jiménez, *A new fractional-order mask for image edge detection based on caputo-fabrizio fractional-order derivative without singular kernel*, Circuits, Syst. Signal Process. **39** (2020) 1419–1448.

[17] D. Marr, E. Hildreth, *Theory of edge detection*, Proc. R. Soc. B: Biol. Sci. **207** (1980) 187–217.

[18] D. Martin, C. Fowlkes, D. Tal, J. Malik, *A database of human segmented natural images and its application to evaluating segmentation algorithms and measuring ecological statistics*, in: Proceedings of the IEEE International Conference on Computer Vision. (2001) 416–425.

[19] B. Mathieu, P. Melchior, A. Oustaloup, C. Ceyral, *Fractional differentiation for edge detection.* Signal Process. Image Commun. **83** (2003) 2421–2432.

[20] G.A.M. Nchama, L.D.L. Alfonso, A.L.M. Galloso, *Caputo and caputo-fabrizio fractional differential masks for images enhancement*, Divulg. Mat. **22** (2021) 1–21.

[21] A. Nandal, H. Gamboa-Rosales, A. Dhaka, J.M. Celaya-Padilla, J.I. Galvan-Tejada, C.E. Galvan-Tejada, F.J. Martinez-Ruiz, C. Guzman-Valdivia, *Image edge detection using fractional calculus with feature and contrast enhancement*, Circuits, Syst. Signal Pro. **37** (2018) 3946–3972.

[22] K.M. Owolabi, A. Atangana, *High-order solvers for space-fractional differential equations with riesz derivative*, Discrete Contin. Dyn. Syst. **12** (2019) 567–590.

[23] S. Pandey, *The Lorenzo-Hartleys function for fractional calculus and its applications pertaining to fractional order modelling of anomalous relaxation in dielectrics*, Comput. Appl. Math. **37** (2018) 2648–2666.

[24] J.M. Prewitt, *Object enhancement and extraction*, Compute. Graph. Image Process **10** (1970) 15–19.

[25] Y.F. Pu, W. Wang, *Fractional differential masks of digital image and their numerical implementation algorithms*, Acta Autom. Sin. **33** (2007) 1128–1135.

[26] Y.F. Pu, J.L. Zhou, X. Yuan, *Fractional differential mask: a fractional differential-based approach for multiscale texture enhancement*, IEEE Trans. Image Process **19** (2009) 491–511.

[27] S. Samko, A.A. Kilbas, O.I. Marichev, *Fractional integrals and derivatives: Theory and applications*, 1993.

[28] I. Sobel, *An isotropic 3×3 image gradient operator*, Presentation at Stanford A.I. Project 1968, 2014.

[29] R. Tawsifur, A. Khandakar, Y. Qiblawey, A. Tahir, S. Kiranyaz, S.B. Abul Kashem, M.T. Islam, S. Al Maadeed, S.M. Zughaier, M.S. Khan, et al. *Exploring the effect of image enhancement techniques on covid-19 detection using chest x-ray images*, Comput. Biol. Med. **132** (2021) 104319.

[30] D. Tian, J. Wu, Y. Yang, *A fractional-order edge detection operator for medical image structure feature extraction*, In: The 26th Chinese Control and Decision Conference (2014) 5173–5176.

[31] M.P. Velasco, D. Usero, S. Jimenez, L. Vazquez, J.L. Vazquez-Poletti, M. Mortazavi, *About some possible implementations of the fractional calculus*, Mathematics **8** (2020) 893.

[32] Q. Yang, D. Chen, T. Zhao, Y. Chen, *Fractional calculus in image processing: a review*, Fract. Calc. Appl. Anal. **19** (2016) 1222–1249.

[33] Q. Yang, Y. Zhang, T. Zhao, Y. Chen, *Single image super-resolution using self-optimizing mask via fractional-order gradient interpolation and reconstruction*, ISA Trans. **82** (2018) 163–171 .